


High-order harmonic generation from twisted bilayer graphene driven by a midinfrared laser fieldMeiwen Du, Candong Liu ,* Zhinan Zeng, and Ruxin Li*State Key Laboratory of High Field Laser Physics and CAS Center for Excellence in Ultra-intense Laser Science, Shanghai Institute of Optics and Fine Mechanics (SIOM), Chinese Academy of Sciences (CAS), Shanghai 201800, China and Center of Materials Science and Optoelectronics Engineering, University of Chinese Academy of Sciences, Beijing 100049, China* (Received 1 April 2021; revised 27 July 2021; accepted 2 September 2021; published 21 September 2021)

Theoretical calculations of high-harmonic generation (HHG) from commensurate twisted bilayer graphene (tBLG) under intense laser fields are performed. The nonlinear electron dynamics in tBLG is considered by solving the Liouville–von Neumann equation for a single-particle density matrix, which combines the full energy bands and momentum matrix elements within the framework of tight-binding approximation. We show that the pump intensity determines the relative magnitude of two components of the harmonic spectrum parallel and perpendicular to driving polarization. The important dependence of HHG on twisted angles and crystal orientations is also presented. Especially in the absence of the relaxation process, the harmonic emission for twisted angles around 10° exhibits an evident decrease in efficiency per layer compared to monolayer graphene (MLG), which can be interpreted according to Fermi velocity modification. Our calculation also shows that the relative emission efficiency of different harmonic orders between tBLG and MLG contains redundant information on both the dephasing time and an empirical parameter characterizing the decay of the interlayer electron hopping, thus suggesting an all-optical method for the reconstruction of the two parameters. The reconstruction feasibility is successfully demonstrated by a simple optimization algorithm even if considering the possible experimental uncertainty of both driving pulse parameters and high-harmonic signals. Our results show that HHG spectroscopic characteristics in tBLG might serve as a fingerprint to identify the geometric stacking angle and the electronic interaction between adjacent layers, as well as the strong-field laser induced ultrafast dephasing process.

DOI: [10.1103/PhysRevA.104.033113](https://doi.org/10.1103/PhysRevA.104.033113)**I. INTRODUCTION**

Since the first observation of high-harmonic generation (HHG) in ZnO crystals [1], there has been a lot of interest in the investigation of the highly nonlinear optical response of solid materials to intense laser fields [2–9]. The subsequent experiments demonstrate HHG can be achieved in various condensed matters driven by intense laser pulses with wavelength ranging from the near infrared to the terahertz. The solid HHG originates from the subcycle electron motion and is strongly dependent on dispersion of energy bands, thus providing potential applications in probing both ultrafast electron dynamics [10] and intrinsic information on electronic structures [11,12]. As a nonlinear frequency up-conversion process, HHG in solids might also serve as a promising coherent radiation source [3,13].

The spatiotemporal symmetries of a laser-solid system determine some general features of HHG, such as selection rules imposed on odd or even harmonics [14], carrier-envelope phase slip of high-harmonic waveforms [15], and the crystal-orientation dependent modulation for the polarization-resolved harmonic spectrum [4]. In addition, HHG in different materials also shows the unique dependence on the waveform and polarization state of the driving pulse, originating from

the diversity of the material lattice and band structure [16,17]. Thus, exploration of HHG from a novel material is helpful in getting deep insight into the microscopic mechanism of this strong-field process.

Twisted bilayer graphene (tBLG) is such an important atomically thin material where the two graphene layers are stacked in an arbitrary orientation. The lattice mismatch between two atomic layers can give rise to additional freedom to manipulate electronic features, resulting in the distinct band structure from pure monolayer graphene (MLG). A large variety of physical phenomena such as the circular photogalvanic effect [18], two-dimensional (2D) higher-order topological insulator [19], and very recently magic-angle superconductivity [20] have been found in the tBLG. The previous investigation about the tBLG is mainly focused on the physical properties around the Fermi level in the low-energy region [21,22]. The nonlinear electronic dynamics in tBLG induced by the intense laser field has not yet been well discussed. The superlattice structure acting as an external periodic potential and the interlayer coupling can modify the ultrafast dynamics in tBLG, particularly for the strong-field driving pulse that can pave carriers across a large part of the Brillouin zone (BZ). It is therefore expected that HHG in tBLG will exhibit novel contents and merit the study on this topic.

The length-gauge semiconductor Bloch equation (SBE) [23–27] is a widely used model to calculate HHG in solids, with the advantage of incorporating real material

*cdliu@siom.ac.cn

parameters and considering relaxation process phenomenologically. The application of the SBE method in tBLG should consider enough energy bands covering a wide energy range to support the high excitation in the strong-field process, which usually involves a large number of bands due to lots of carbon atoms in the superlattice unit cell. This situation poses a theoretical challenge, especially for the small-twisted-angle tBLG, since the number of atoms in the unit cell increases rapidly with decreasing twisted angle. It has been demonstrated that the correct treatment of the phase of transition dipole moments [28,29] is important for calculating high harmonics with the length-gauge SBE. This is usually difficult to implement for a tBLG system where numerous electronic bands are formed in the folded BZ compared with the MLG. Another theoretical difficulty is that energy bands far away from the Fermi level will be closer, which easily leads to the singularity of transition dipole moments owing to its value inversely proportional to the band gap.

In this work, we calculate HHG in tBLG using our previous theoretical model that has been successfully applied to MoS₂ [30]. The tight-binding approximation is employed to construct the field-free Hamiltonian. We consider the complete tBLG electronic structures instead of the widely used low-energy continuum model [22] where only a few bands are touched. The carrier dynamics in a midinfrared intense field is treated with the Liouville–von Neumann equation in the velocity gauge. Our model has a good numerical stability even if all valence and conduction bands are included. The phase continuous issue is automatically solved, since in the model transition dipole moments are replaced with momentum matrix elements, whose phase can be chosen in an arbitrary way.

Another alternative theoretical model is the time-dependent Schrödinger equation (TDSE) in the Fourier representation. Ikeda has successfully applied it [31] in the simulation of high-order nonlinear optical response of the minimal commensurate tBLG and found rich characteristics in the high-harmonic spectrum. Another velocity-gauge TDSE has also been developed in Ref. [32]. In the absence of electron–electron interactions, dephasing, and energy relaxation processes, the Liouville–von Neumann equation is fully equivalent to a set of the single-particle TDSE, where an electron is initially occupying one of the valence band states. The unphysical transitions forbidden by the Pauli principle are canceled out after the summation of contributions from all the single-particle equations. Thus, both methods can not only avoid the phase and numerical instability issue, but also properly take into account the Pauli blocking of interband transitions [33]. However, our method enables us to introduce the dephasing effect phenomenologically, and provides the opportunity to investigate the relaxation influence on HHG in tBLG. Moreover, we discuss the crystal-orientation-dependent and twisted-angle-dependent HHG in tBLG. According to the calculated spectrum, we propose an all-optical method for the reconstruction of the dephasing time and the interlayer electron hopping.

II. THEORETICAL METHODS

We consider the lattice structure of tBLG, starting from a perfect AB stacked form where one of the two sublattices of

one layer sites in the center of the honeycomb structure of the other layer. The tBLG is then obtained by rotating the top layer with respect to the bottom layer around the axis passing through a pair of coincident carbon atom sites. If the rotation operation produces a superlattice of tBLG, which is a periodical lattice of supercells, the formed tBLG is commensurate. This commensurate structure that maintains the translation symmetry is more suitable for a theoretical description of electronic properties. Thus, we mainly focus on HHG from the commensurate tBLG in this work. It has been derived that the commensurate rotation angle should satisfy [34]

$$\cos \theta = \frac{3m^2 + 3mr + r^2/2}{3m^2 + 3mr + r^2}, \quad (1)$$

where m and r are coprime positive integers.

The basis vectors (α_1, α_2) of the commensurate superstructure can be constructed by the linear combination of two single-layer graphene lattice vectors ($\mathbf{a}_1, \mathbf{a}_2$) in the form of $\alpha = \mathbf{T}(m, n)\mathbf{a}$, using the column vector symbol $\alpha = (\alpha_1, \alpha_2)^T$ and $\mathbf{a} = (\mathbf{a}_1, \mathbf{a}_2)^T$. $\mathbf{T}(m, n)$ is a 2×2 transform matrix, whose explicit expression is written as

$$\mathbf{T}(m, n) = \begin{pmatrix} m & m+r \\ -m-r & 2m+r \end{pmatrix}, \quad (2)$$

if $r \neq 3n$, $n \in \mathbb{N}$, or

$$\mathbf{T}(m, n) = \begin{pmatrix} m+n & n \\ -n & m+2n \end{pmatrix}, \quad (3)$$

if $r = 3n$, $n \in \mathbb{N}$. Here, $\mathbf{a}_1 = \frac{a}{2}(1, \sqrt{3})$ and $\mathbf{a}_2 = \frac{a}{2}(-1, \sqrt{3})$ are the two primitive lattice vectors of the bottom-layer graphene, with the lattice constant $a = 2.46 \text{ \AA}$. The above basis vectors can be illustrated in terms of the minimal commensurate tBLG with a twisted angle $\theta \approx 21.8^\circ$, generated by $m = 1$ and $r = 1$, as shown in Fig. 1(a), where the blue (red) solid circles represent the bottom (top) layer carbon atoms. We also plot the corresponding reciprocal space in Fig. 1(b), which shows that the first Brillouin zone (BZ) of the top layer (blue-dashed hexagon) rotates $\theta \approx 21.8^\circ$ anticlockwise relative to that of the bottom layer (red-dashed hexagon). For the special case of $r = 1$, the vector connecting the top layer Dirac point K and the bottom layer Dirac point K_θ is equal to one side of the superlattice BZ, with the first BZ given by the central solid hexagon in Fig. 1(b). The reciprocal lattice primitive vectors can be chosen as

$$\begin{pmatrix} \mathbf{G}_1 \\ \mathbf{G}_2 \end{pmatrix} = \frac{4\pi}{3|\alpha_1|^2} \begin{pmatrix} 2 & -1 \\ -1 & 2 \end{pmatrix} \begin{pmatrix} \alpha_1 \\ \alpha_2 \end{pmatrix}. \quad (4)$$

We use the tight-binding (TB) model to describe electronic states of the tBLG by taking account of the carbon $2p_z$ orbital of electrons in the two graphene layers. The basis function used to expand electronic eigenstates can be constructed by the Bloch sum of atomic orbits as

$$B_i(\mathbf{k}, \mathbf{r}) = \frac{1}{\sqrt{N}} \sum_{\mathbf{R}} e^{i\mathbf{k} \cdot (\mathbf{R} + \boldsymbol{\tau}_i)} \varphi_{p_z}(\mathbf{r} - \mathbf{R} - \boldsymbol{\tau}_i), \quad (5)$$

where the sum runs over the supercell lattice vectors $\mathbf{R} = m_1\alpha_1 + m_2\alpha_2$, and there are N superlattice sites in the crystal. Here, i labels one atom in the primary supercell, and $\boldsymbol{\tau}_i$ is the

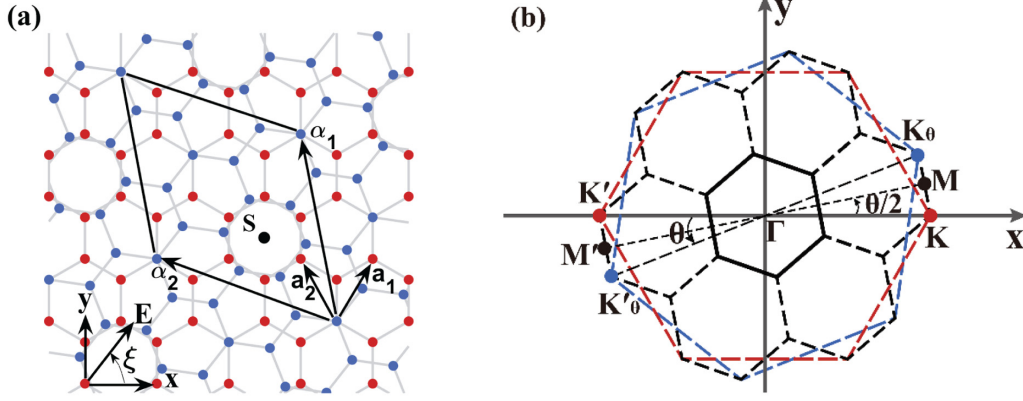


FIG. 1. (a) Top view of the commensurate tBLG lattice structure with a twisted angle of $\theta \approx 21.8^\circ$ ($m = 1$, $r = 1$). \mathbf{a}_1 and \mathbf{a}_2 are the primitive vectors of the bottom layer graphene. α_1 and α_2 are the basis vectors of the superlattice. (b) Schematic of the BZ corresponding to panel (a). The red-dashed larger hexagon represents the first BZ of the bottom layer with two inequivalent Dirac points K, K' . The blue-dashed hexagon, which rotates $\theta \approx 21.8^\circ$ counterclockwise relative to the red-dashed one, is the first BZ of the top layer with two inequivalent Dirac points K_θ, K'_θ . The seven smaller hexagons in black are the BZ of superlattice tBLG. M and M' are the middle points of the BZ side $K - K_\theta$ and $K' - K'_\theta$, respectively.

location of atom i with respect to the origin of the supercell. We can express the TB eigenstate of the tBLG as

$$|n, \mathbf{k}\rangle = \sum_i c_{n,i}(\mathbf{k}) |B_i(\mathbf{k})\rangle, \quad (6)$$

where n represents the band index, and \mathbf{k} is the crystal momentum in the superlattice BZ. The corresponding matrix elements of the field-free unperturbed Hamiltonian H_0 are given by

$$H_{ij}(\mathbf{k}) = \langle B_i | H_0 | B_j \rangle = \sum_{\mathbf{R}} e^{i\mathbf{k} \cdot \mathbf{R}_{ij}} \langle \phi_{p_z}(\mathbf{r}) | H | \phi_{p_z}(\mathbf{r} - \mathbf{R}_{ij}) \rangle, \quad (7)$$

where $\mathbf{R}_{ij} = \mathbf{R} + \boldsymbol{\tau}_{ij}$, and $\boldsymbol{\tau}_{ij} = \boldsymbol{\tau}_j - \boldsymbol{\tau}_i$ represents the vector from atom i pointing to atom j in a unit cell.

The matrix elements $H_{ij}(\mathbf{k})$ can be classified into two categories in our calculation, according to whether atom i and atom j are in the same layer or not:

(1) When two atoms are in the same layer, we neglect the on-site energies and only consider the in-plane nearest-neighbor hopping. In this case, only those terms satisfying $|\mathbf{R}_{ij}| = a_{cc}$ are retained for the summation over \mathbf{R} in Eq. (7), where $a_{cc} = 1.42 \text{ \AA}$ is the nearest carbon-carbon distance in the MLG. We denote the nearest-neighbor hopping energy of p_z electrons as $V_{pp\pi}^0 = \langle \phi_{p_z}(\mathbf{r}) | \mathbf{H}_0 | \phi_{p_z}(\mathbf{r} - \mathbf{R}_{ij}) \rangle$ with $|\mathbf{R}_{ij}| = a_{cc}$.

(2) When two atoms are in different layers, the hopping integral between atom i and atom j is calculated by the following formula based on the Slater-Koster mechanism [35]:

$$\begin{aligned} & \langle \phi_{p_z}(\mathbf{r}) | \mathbf{H}_0 | \phi_{p_z}(\mathbf{r} - \mathbf{R}_{ij}) \rangle \\ &= V_{pp\pi}^0 \exp\left(-\frac{|\mathbf{R}_{ij}| - a_{cc}}{\lambda}\right) \left[1 - \left(\frac{\mathbf{R}_{ij} \cdot \mathbf{e}_z}{|\mathbf{R}_{ij}|}\right)^2\right] \\ &+ V_{pp\sigma}^0 \exp\left(-\frac{|\mathbf{R}_{ij}| - d_0}{\lambda}\right) \left(\frac{\mathbf{R}_{ij} \cdot \mathbf{e}_z}{|\mathbf{R}_{ij}|}\right)^2, \end{aligned} \quad (8)$$

where $V_{pp\sigma}^0$ is the hopping integral for two vertically located atoms in the adjacent layers, d_0 is the distance between the two graphene layers, λ modulates the decay of hopping integral at the large distance, and \mathbf{e}_z is the unit vector perpendicular to the tBLG plane. These parameter values are taken from Ref. [36], i.e., $V_{pp\pi}^0 = -3.03 \text{ eV}$, $V_{pp\sigma}^0 = 0.39 \text{ eV}$, $d_0 = 3.35 \text{ \AA}$, and $\lambda = 0.27 \text{ \AA}$.

If the overlap matrix formed by the basis function $B_i(\mathbf{k}, \mathbf{r})$ is approximated by the unit matrix, the direct diagonalization of $H_{ij}(\mathbf{k})$ can simultaneously yield the energy band $E_n(k)$ and the corresponding eigenstate characterized by expansion coefficients $c_{n,i}(\mathbf{k})$ in Eq. (6). In our work, we perform the full diagonalization algorithm to obtain complete set of eigenstates of Hamiltonian matrix. This is important for the investigation of electronic dynamics in the strong-field regime since the electron can be subjected to the higher excitation and their Bloch motion can extend to the larger range. We have examined the electronic structure model by calculating energy bands of several tBLGs with different twisted angles. The calculated band structures are shown in the Appendix. Note that our model can support the first magic angle $\theta \approx 1.08^\circ$ at which band flattening occurs.

We model the dynamical interaction of tBLG with a laser pulse under the mean-field approximation by density-matrix equations, which can take into account Pauli blocking of interband transitions [33]. The temporal evolution of density-matrix elements in the velocity gauge and within the dipole approximation reads [30]

$$\begin{aligned} \frac{d\rho_{mn}(\mathbf{k}, t)}{dt} &= -i[E_m(\mathbf{k}) - E_n(\mathbf{k})]\rho_{mn}(\mathbf{k}, t) \\ &- i\mathbf{A}(t) \cdot [\hat{\mathbf{p}}(\mathbf{k}), \hat{\rho}]_{mn} + \left. \frac{d\rho(\mathbf{k}, t)}{dt} \right|_{\text{decoh}}, \end{aligned} \quad (9)$$

where $\hat{\rho}$ is the density matrix comprising elements $\rho_{mn}(\mathbf{k}, t) = \langle m, \mathbf{k} | \rho | n, \mathbf{k} \rangle$, and $\mathbf{A}(t)$ is the vector potential of the driving laser field. Unless otherwise indicated, atomic units (a.u.) are used throughout: $e = \hbar = m_e = 1$, where e and m_e are the electron charge and mass, respectively. The

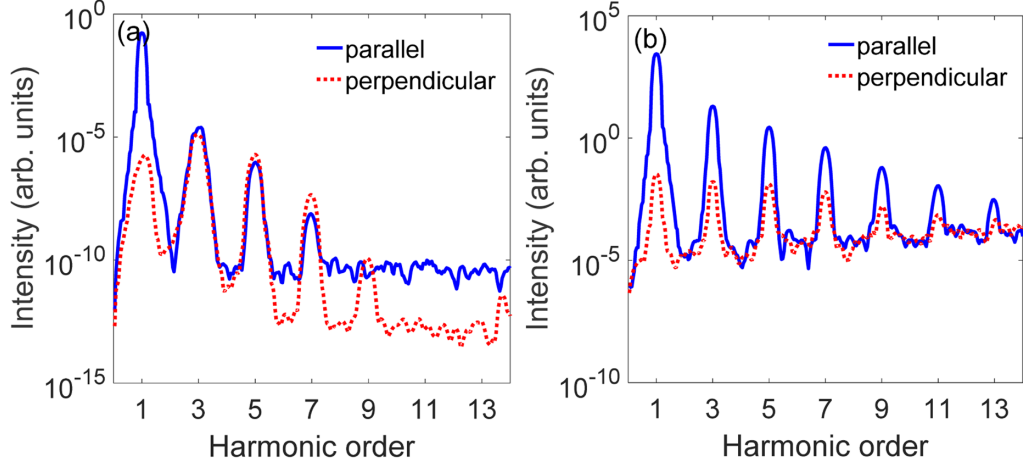


FIG. 2. The parallel (blue solid) and perpendicular (red dashed) polarization components of the high-harmonic spectrum in tBLG with a twisted angle $\theta \approx 21.8^\circ$ under the pulse intensity of (a) $I = 8.5 \times 10^8 \text{ W/cm}^2$ and (b) $I = 3 \times 10^{12} \text{ W/cm}^2$. The Gaussian pump pulse has a central wavelength of 4700 nm, a duration of 90 fs, and is linearly polarized along the x axis in Fig. 1(a).

scattering parts beyond the mean-field approximation are phenomenologically included via the last term of Eq. (9), with the specific form discussed later. The momentum matrix $\hat{\mathbf{p}}(\mathbf{k})$ consists of the element $\mathbf{p}_{mn}(\mathbf{k}) = \langle m, \mathbf{k} | \mathbf{p} | n, \mathbf{k} \rangle$, whose analytical expression can be obtained within the TB approximation as [37]

$$\mathbf{p}_{mn}(\mathbf{k}) = \sum_{ij} c_{m,i}^*(\mathbf{k}) c_{n,j}(\mathbf{k}) \nabla_{\mathbf{k}} H_{ij}(\mathbf{k}). \quad (10)$$

We note that the term of intra-atomic dipole contribution is exactly zero here and therefore is removed, due to the fact that only the p_z orbital is considered for each carbon atom site.

Making use of \mathbf{k} as a parameter to propagate Eq. (9), we can obtain the \mathbf{k} -resolved time-dependent current density,

$$\mathbf{j}_{\mathbf{k}}(t) \propto \text{Tr}\{\hat{\rho}[\hat{\mathbf{p}} + \mathbf{A}(t)]\} = \sum_{mn} \mathbf{p}_{mn}(\mathbf{k}) \rho_{nm}(\mathbf{k}, t) + N_{vb} \mathbf{A}(t), \quad (11)$$

where Tr denotes trace, and N_{vb} is the number of valence bands. The integral of $\mathbf{j}_{\mathbf{k}}(t)$ over the first BZ can give the total current density,

$$\mathbf{J}(t) \propto \int_{\text{BZ}} \mathbf{j}_{\mathbf{k}}(t) d^2\mathbf{k}. \quad (12)$$

The resulting HHG spectrum $I(\omega)$ is obtained by performing the Fourier integral of $\mathbf{J}(t)$ as

$$I(\omega) \propto \left| \omega \int \exp(i\omega t) \mathbf{J}(t) dt \right|^2. \quad (13)$$

Equation (9) is numerically solved for each independent \mathbf{k} by the classical fourth-order Runge-Kutta method combined with an adaptive step-size routine. We choose the first BZ spanned by the primitive reciprocal vectors, and sample \mathbf{k} points with uniform grid spacing along two nonorthogonal directions \mathbf{G}_1 and \mathbf{G}_2 . The grid interval of crystal momentum is fixed to $\delta k = 0.008$ a. u. The evolution time step is initially set as $\delta t = 0.07$ fs, which could be shortened by the adaptive algorithm in order to meet the required accuracy within $\varepsilon = 10^{-6}$. The simulation convergence has been checked by the comparison of results obtained with decreasing δk and ε .

III. RESULTS AND DISCUSSION

A. Crystal-orientation-dependent HHG from tBLG

The driving laser intensity is an important parameter that affects the excitation of electrons from valence band to conduction band, which could lead to the competition between the interband- and intraband-mechanism HHG. Thus, we have observed the general feature of the harmonic spectrum from the minimal commensurate tBLG driven by both weak and strong pump intensity. A linearly polarized midinfrared (MIR) driving pulse is employed, with a central wavelength of 4700 nm and a pulse duration of 90 fs in the Gaussian envelope. We neglect the relaxation progress in this section, and their influence will be discussed in Sec. III C.

Figure 2(a) shows the polarization-resolved high-harmonic spectrum generated for a driving pulse having a relatively weak peak intensity of $8.5 \times 10^8 \text{ W/cm}^2$. Here, the blue solid and red dashed lines represent the harmonic component perpendicular and parallel to the polarization of the driving pulse, respectively. In the calculation, the driving pulse is polarized along the x -axis direction [see Fig. 1(a)], i.e., $\xi = 0^\circ$, which belongs to a non-high-symmetry crystal orientation. One can see from Fig. 2(a) that discrete and clean odd harmonics are present, with the comparable intensity for the parallel and perpendicular component. The absence of even harmonics originates from the structures that are even under sublattice exchange (SE) [22], making an inversion symmetry with respect to such as the S point shown in Fig. 1(a). Note that our result is different from Ref. [31], where perpendicular even harmonics are observed. This is due to the fact that the lattice structure used in Ref. [31] is SE odd, corresponding to twist angle $\theta \approx 38.2^\circ$ produced from $m = 1$ and $r = 3$ in our notation, and thus lacks inversion centers.

We then increase the driving pulse intensity to $3.0 \times 10^{12} \text{ W/cm}^2$, and keep other laser parameters unchanged. Figure 2(b) shows the harmonic spectrum in a direction parallel (red dashed line) and perpendicular (solid blue line) to the polarization of the driving pulse. The obvious difference from Fig. 2(a) is that the parallel component dominates the

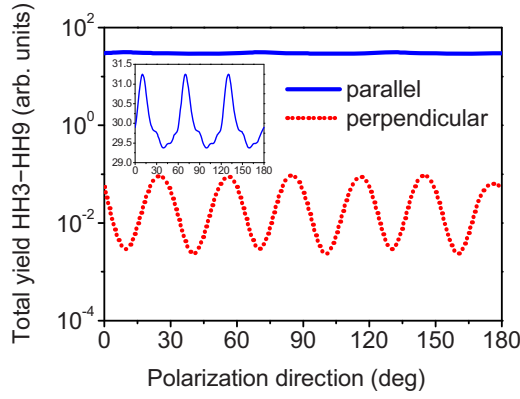


FIG. 3. The total yield of the high-harmonic spectrum from the third to the ninth order as a function of polarization direction ξ , calculated for two components parallel (blue solid) and perpendicular (red dashed) to the driving polarization. The inset shows the ξ -dependent parallel component plotted on a linear scale. The laser parameters are the same as in Fig. 2(b).

harmonic emission, while the perpendicular component can be negligible for the strong pump intensity. For the same laser intensity, we further calculate the total harmonic yield upon varying the crystal orientation, which is described by the polar angle ξ of driving polarization [see Fig. 1(a)]. Figure 3 shows the total yield of parallel (solid blue) and perpendicular (dashed red) harmonic component as a function of the polarization angle ξ ranging from 0° to 180° . Here, the yield is defined as integrating the spectrum from the third to the ninth harmonic order. It is found that the parallel emission is always dominate for arbitrary crystal orientation, with its yield nearly three orders of magnitude larger than the perpendicular component. In addition, as more clearly seen with a linear scale by the inset of Fig. 3, the parallel harmonics exhibit 60° modulation with changing crystal orientation, reflecting the sixfold rotation symmetry of the tBLG lattice. In contrast, the perpendicular harmonics shown in Fig. 3 are deeply modulated with a period of 30° , and similar modulation behavior has also been observed experimentally in other materials, such as bulk GaSe [9] and topological insulator surface [38]. They might have the same physical origin, which is attributed to anisotropic momentum dependence of the band curvature [9].

We now turn to the investigation of the crystal-orientation-dependent characteristics for different structures of tBLG, taking the fifth-harmonic order (HH5) as a representative and study its modulation behavior in detail. It has been demonstrated that the other odd harmonics represent the same result. In the typical experiment of HHG from 2D materials [4,6], the driving pulse intensity is usually at the order of a few TW/cm². For providing a guide for possible experimental observation, we only choose the strong pump intensity from here on. Thus, it is not necessary to consider two orthogonal polarization components separately as above, since the perpendicular emission is too weak to be observed, as reported in Fig. 3. For simplicity, we directly work with the total HH5 yield.

Figure 4 shows the HH5 yield as a function of polarization direction ξ of the driving pulse, calculated for tBLGs with different twist angles: $\theta \approx 21.8^\circ$ (olive dash-dotted), $\theta \approx 13.2^\circ$

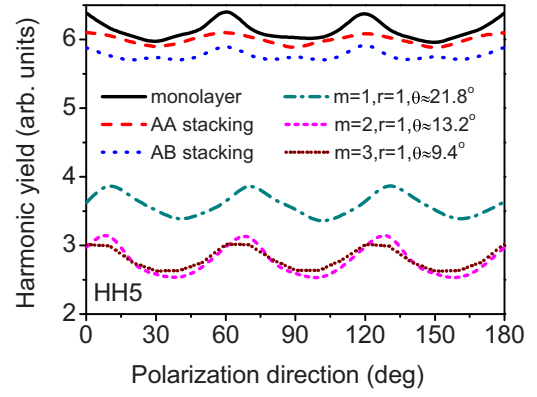


FIG. 4. The fifth-order average harmonic yield per layer as a function of the polarization angle ξ , calculated for the conventional AA (red dashed) and AB stacking (blue dotted) bilayer graphene, as well as the SE-even tBLGs with twist angle $\theta \approx 21.8^\circ$ (olive dash-dotted), $\theta \approx 13.2^\circ$ (magenta short-dashed), and $\theta \approx 9.4^\circ$ (wine short-dotted), respectively. For comparison, the result for the MLG with the same lattice arrangement as the bottom layer of tBLG is also plotted by a black solid line. Laser parameters are the same as in Fig. 2(b).

(magenta short-dashed), and $\theta \approx 9.4^\circ$ (wine short-dotted). Here, we mainly focus on typical tBLGs with $r = 1$, since structures with $r > 1$ are almost-periodic repetitions of the $r = 1$ family [39]. Calculations toward the smaller twist angle (larger m) are cut down due to the time-consuming simulation. For comparison, we also calculate the HH5 modulation for the MLG (black solid), together with the conventional bilayer AA stacking (red dashed) and AB stacking (blue dotted) graphene, as shown in Fig. 4. Note that the lattice arrangement of MLG is the same as the bottom layer of tBLG. For all bilayer cases, the calculated yield has already been divided by 2, reflecting the average yield per layer.

A common sixfold rotational periodicity is observed for these six curves in Fig. 4, although their modulation depths differ from each other. Specifically, the maximal yield for the MLG occurs at the polarization direction $\xi = 60^\circ \times n$, corresponding to the Γ - K direction in the momentum space. This is because Dirac cones at the K point play a dominant role in this intense nonlinear process [40]. The modulation in conventional AA and AB stacking bilayers is in phase with the MLG since their BZs hold the same orientation and symmetry. However, there is a phase shift between MLG and tBLGs with different twisted angle θ . The phase shift can be directly extracted from Fig. 4 and is found to be $\theta/2$, resulting in such situation that the maximum harmonic yield is obtained for the driving polarization along the Γ - M direction as shown in Fig. 1(b). The feature can be simply interpreted in terms of the interference of harmonic emission from each layer of tBLG, as follows:

First, using Eqs. (10)–(12), we can rewrite the total current density in the form of

$$\mathbf{J}(t) \propto \sum_{ij} \int_{\text{BZ}} \sum_{mn} c_{m,i}^*(\mathbf{k}) c_{n,j}(\mathbf{k}) \nabla_{\mathbf{k}} H_{ij}(\mathbf{k}) \rho_{nm}(\mathbf{k}, t) d^2\mathbf{k}, \quad (14)$$

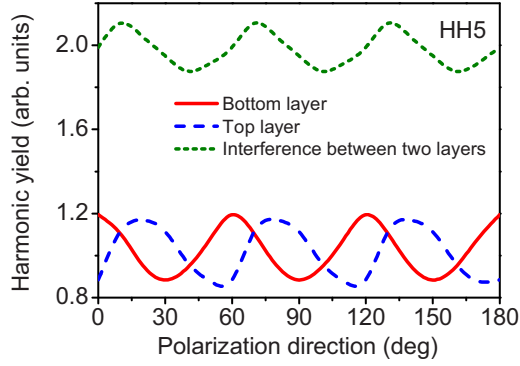


FIG. 5. The fifth-order harmonic yield in tBLG ($m = 1$, $r = 1$) as a function of polarization angle ξ , obtained from the contribution of bottom-layer current (red solid), top-layer current (blue dashed), and interference between two layers (olive short-dashed). Laser parameters are the same as in Fig. 2(b).

where we drop the $N_{vb}\mathbf{A}(t)$ term since it does not contribute to high harmonics. The outermost summation in Eq. (14) can be divided into three parts according to whether atom i and atom j are in the same layer (bottom or top) or not:

$$\sum_{ij} = \sum_{i,j \in \text{top}} + \sum_{i,j \in \text{bottom}} + \sum_{\substack{i \in \text{bottom}, j \in \text{top} \\ i \in \text{top}, j \in \text{bottom}}} . \quad (15)$$

Therefore, the total current density can be naturally decomposed into three parts:

$$\mathbf{J}(t) = \mathbf{J}_1(t) + \mathbf{J}_2(t) + \mathbf{J}_3(t), \quad (16)$$

where $\mathbf{J}_1(t)$ represents the top-layer current, $\mathbf{J}_2(t)$ represents the bottom-layer current, and $\mathbf{J}_3(t)$ represents the interlayer current.

Then we choose the minimal commensurate tBLG described by $m = 1$ and $r = 1$ as representative, and numerically estimate the contribution of each current component in Eq. (16) to HHG. We find that the intensity of harmonics induced by $\mathbf{J}_3(t)$ is almost four orders of magnitude lower than the one induced by $\mathbf{J}_1(t)$ or $\mathbf{J}_2(t)$, so that the $\mathbf{J}_3(t)$ component can be safely neglected. We denote the Fourier transformation of $\mathbf{J}_1(t)$ and $\mathbf{J}_2(t)$ as $\mathbf{h}_1(\omega)$ and $\mathbf{h}_2(\omega)$, respectively. Consequently, the total high-harmonic spectrum can be expressed as

$$I(\omega) = |\mathbf{h}_1(\omega)|^2 + |\mathbf{h}_2(\omega)|^2 + 2\text{Re}[\mathbf{h}_1(\omega) \cdot \mathbf{h}_2(\omega)^*], \quad (17)$$

where the first two terms represent the incoherent sum of HHG from the top and bottom layers, and the last term represents the interference between two layers.

We can calculate each term in Eq. (17) upon scanning the polarization direction of the driving pulse. Figure 5 shows the HH5 yield as a function of polarization direction, obtained from the top layer $|\mathbf{h}_1(\omega)|^2$ (blue dashed), the bottom layer $|\mathbf{h}_2(\omega)|^2$ (red solid), and their interference $2\text{Re}[\mathbf{h}_1(\omega) \cdot \mathbf{h}_2(\omega)^*]$ (olive short-dashed). One can see from Fig. 5 that the interference of two single-layer harmonic emission is important, and its phase shift relative to the bottom emission is exactly equal to $\theta/2$, where θ is the twisted angle. For the single-layer yield alone, the maximal position occurs at $\xi = 60^\circ \times n$ for the bottom emission and $\xi = 60^\circ \times n + \theta$

TABLE I. Commensurate tBLG structures. N is the number of atom sites in a primitive cell.

N	SE even [θ (m , r)]	SE odd [θ (m , r)]
28	[21.8° (1, 1)]	[38.2° (1, 3)]
76	[13.2° (2, 1)]	[46.7° (1, 6)]
148	[9.4° (3, 1)]	[50.6° (1, 9)]
244	[7.3° (4, 1)]	[52.7° (1, 12)]

for the top emission, corresponding to the Γ - K direction of each respective momentum space. These results can guide us to further qualitatively consider the incoherent process.

For the bottom layer in tBLG, similar to the monolayer case, the harmonic yield y_1 as a function of the polarization angle ξ can be expressed as

$$y_1 = C_1 + C_2 \cos 6\xi. \quad (18)$$

For the top layer, its BZ suffers from a counterclockwise rotation angle θ , so that a phase shift θ should be added to the ξ , and therefore its harmonic yield y_2 is given by

$$y_2 = C_1 + C_2 \cos[6(\xi - \theta)]. \quad (19)$$

The average yield per layer in tBLG can be derived with the superposition of these two layers:

$$y = (y_1 + y_2)/2 = C_1 + C_2 \cos(3\theta) \cos\left[6\left(\xi - \frac{\theta}{2}\right)\right]. \quad (20)$$

It is evident that there is a phase shift of $\theta/2$ in the incoherent yield sum, as described by the latter oscillating term of Eq. (20), which is the same as the one involved in the interference term $2\text{Re}[\mathbf{h}_1(\omega) \cdot \mathbf{h}_2(\omega)^*]$. Thus we can conclude that the total harmonic yield should have the same phase shift of $\theta/2$, in accordance with our simulated results.

B. HHG efficiency analysis with different twist angles

To analyze the HHG efficiency, we introduce a harmonic yield ratio between the tBLG and MLG, which is defined as

$$R_N(\theta) = \frac{Y_{2,N}(\xi_2, \theta)}{Y_{1,N}(\xi_1)}, \quad (21)$$

where N denotes the harmonic order, ξ_1 (ξ_2) is the polarization angle of the pump pulses, $Y_{1,N}(\xi_1)$ is the N th harmonic yield in the MLG, and $Y_{2,N}(\xi_2, \theta)$ is the N th harmonic average yield per layer in bilayers with twist angle θ . The ξ_1 and ξ_2 are always chosen to make $Y_{1,N}(\xi_1)$ and $Y_{2,N}(\xi_2, \theta)$ reach maximum, respectively. We mainly focus on the range of the twist angle θ from 0° to 60° . Note that $\theta = 0^\circ$ and $\theta = 60^\circ$ correspond to conventional AB and AA stacking, respectively. To reduce the computation cost for tBLG, we select four SE-even structures ($r = 1$, $m = 1, 2, 3, 4$) generating angles $0^\circ < \theta < 30^\circ$, and the accompanying four SE-odd structures ($m = 1$, $r = 3, 6, 9, 12$) generating angles $30^\circ < \theta < 60^\circ$. The twist angle and the number of atom sites in a primitive cell for these used tBLGs are listed in Table I. The third (HH3), fifth (HH5), seventh (HH7), and ninth (HH9) odd harmonics are taken into account for their sufficient yield in the case of using strong pump intensity.

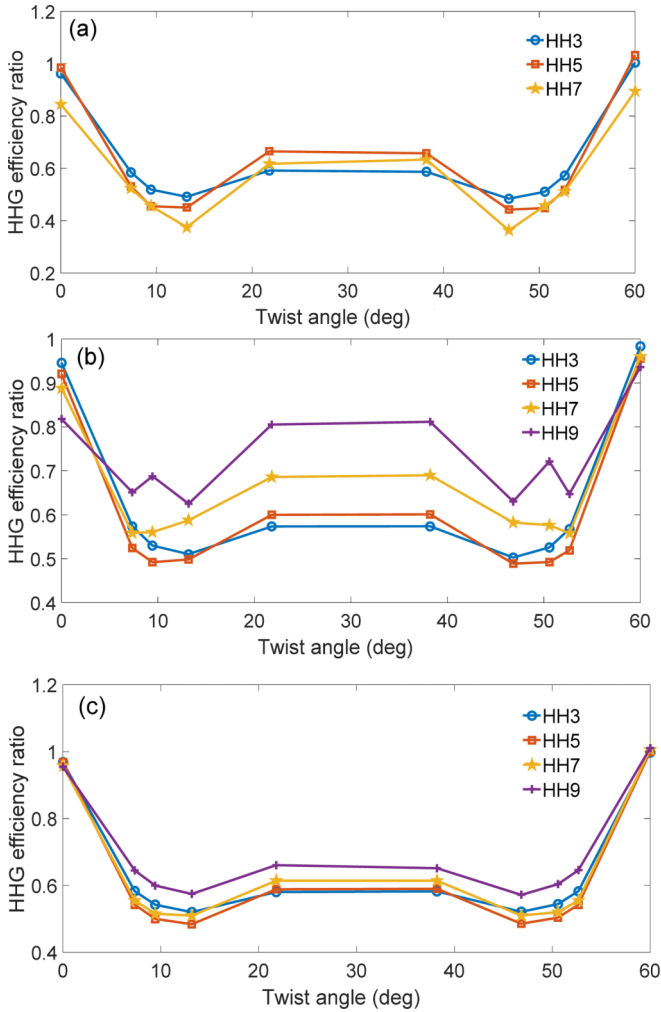


FIG. 6. The HHG efficiency ratio $R_N(\theta)$ as a function of the twist angle θ under three different pump wavelengths: (a) 3500, (b) 4700, and (c) 5900 nm, calculated for the third (blue circles, HH3), fifth (red squares, HH5), seventh (orange stars, HH7), and ninth (purple pluses, HH9) orders. For each case, the pump intensity is fixed at $I = 3 \times 10^{12}$ W/cm² and the pulse duration is set as 90 fs. The dephasing process is not considered.

Figure 6(b) shows the HHG efficiency ratio as a function of the twist angle, calculated for HH3 (blue circles), HH5 (red squares), HH7 (orange stars), and HH9 (purple pluses). The wavelength of the fundamental pulse is 4700 nm. It is clear that each curve is symmetric about $\theta = 30^\circ$, suggesting that variation tendencies of the SE-even and SE-odd family are the same. Consequently, we restrict our statement for the HHG efficiency ratio in a range from 0° to 30° . All curves in Fig. 6(b) are below 1, indicating a loss of harmonic emission efficiency at the existence of a twist angle. However, the conventional AB and AA stacking bilayer graphene exhibit the comparable HHG efficiency to the monolayer graphene. Another feature in Fig. 6(b) is that all harmonic orders share almost the same nonmonotonic behavior with changing twist angle. The curves drop rapidly at the small angle from 0° to about 10° , followed by a slow rise at the large angle until 30° . These two types of variation can be qualitatively understood by two different mechanisms: (i) multiband effect

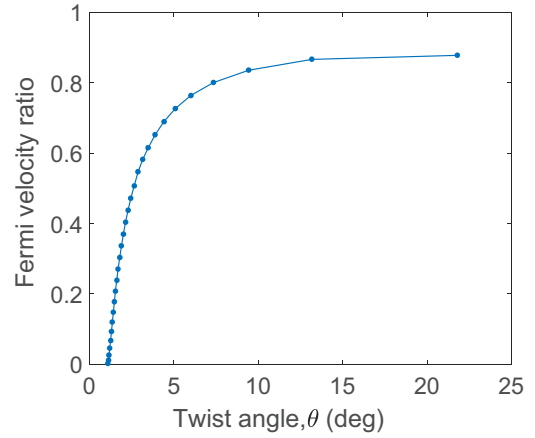


FIG. 7. The Fermi velocity ratio $\bar{v}_F(\theta)$ in tBLGs as a function of the twist angle θ , which is generated for the $r = 1$ family by varying m from $m = 1$ ($\theta \approx 21.8^\circ$) to $m = 30$ ($\theta \approx 1.08^\circ$).

at small angles and (ii) Fermi velocity modification at large angles.

At small angles, the band structure of tBLGs shows more dense distribution due to the BZ folded in comparison with the monolayer case (see the Appendix). More conduction and valence bands are gathered in the vicinity of the Fermi level as the twist angle decreases from $\theta = 10^\circ$ to $\theta = 0^\circ$, so that electron excitation to the higher band is possible during the strong-field interaction process. Thus the harmonic emission is strongly enhanced due to the multiband effect, well consistent with the notably rising part from $\theta = 10^\circ$ to $\theta = 0^\circ$ in Fig. 6(b).

At large angles, however, the multiband effect is markedly reduced because energy bands are well separated. Consequently, the dynamics of tBLG exposed in a MIR laser field can be approximately governed by one valence and one conduction band at both sides of the Fermi level. For the two-band model, the Fermi velocity that is related to off-diagonal elements of the effective Hamiltonian matrix can determine the induced harmonic current, i.e., the HHG efficiency [22,41]. Here we introduce the Fermi velocity ratio, defined as $\bar{v}_F(\theta) = v_F(\theta)/v_{F0}$, where $v_F(\theta)$ and v_{F0} are the Fermi velocity in tBLG and MLG, respectively.

The theoretical evaluation of the $v_F(\theta)$ is based on the approximate equation of linear dispersion around the Dirac point \mathbf{K}_D :

$$E_{\pm}(\mathbf{q}) = \pm v_F(\theta)|\mathbf{q}| + \mu, \quad (22)$$

where $\mathbf{q} = \mathbf{k} - \mathbf{K}_D$ is the crystal momentum measured relative to \mathbf{K}_D . The fitting of the exact calculated data for the uppermost valence and the lowest conduction band to Eq. (22) can yield $v_F(\theta)$. In the calculation, we use tBLG of the $r = 1$ family and vary m from $m = 1$ to $m = 30$. The obtained Fermi velocity ratio $\bar{v}_F(\theta)$ as a function of the twist angle is plotted in Fig. 7. For the angle decreasing from $\theta = 21.8^\circ$ to the vicinity of $\theta = 10^\circ$, it can be seen that the Fermi velocity ratio gradually falls off, well consistent with the slow decline of the HHG efficiency during that angle range as shown in Fig. 6(b). The suppressed coherent interlayer hopping at low energy, arising from the momentum mismatch between the Dirac

cones in different layers [21], results in the twisted-angle-dependent Fermi velocity in tBLG and therefore is responsible for the reduction of the HHG efficiency.

We also alter the wavelength of the driving pulse to calculate the twisted-angle-dependent HHG efficiency ratio. Figures 6(a) and 6(c) illustrate the results with a pulse at 3500 and 5900 nm, respectively. The HH9 in the 3500 nm case is removed because of reaching the cutoff. The variation of the HHG efficiency ratio in Figs. 6(a) and 6(c) exhibits a similar nonmonotonical tendency as results reported in Fig. 6(b). In Figs. 6(a)–6(c), the twist angle where the efficiency ratio reaches the minimum lies commonly in a range between 10° and 15° , with a slight shift dependent on the wavelength. We can therefore conclude that the driving wavelength has little effect on the HHG efficiency.

C. Effect of dephasing time and interlayer coupling

In the preceding sections, we mainly study the purely coherent dynamics in tBLG. It has been demonstrated both theoretically and experimentally [1,2,4,42] that the dephasing process is significant for HHG. It is therefore worth exploring the impact of dephasing on HHG from tBLG.

We start by estimating the validity of Markov approximation in our case [43]. It has been identified that the exciton binding energy in tBLG scales from 0.5 to 0.7 eV [44] and the maximum phonon energy extracted from Ref. [45] is about 34 meV. The maximum kinetic energy of an electron driven by the laser field can be estimated by analyzing the intraband current [3], which is defined as $\mathbf{J}_{ra}(t) \propto \int_{\text{BZ}} \sum_n f_n(\mathbf{k}, t) \nabla_{\mathbf{k}} E_n[\mathbf{k} + \mathbf{A}(t)] d^2\mathbf{k}$. For tBLG ($m = 1, r = 1$) driven by the $4700 \text{ nm}/3.0 \times 10^{12} \text{ W/cm}^2$ laser pulse, we can clearly observe the strong Fourier frequency component of $\mathbf{J}_{ra}(t)$ up to the 15th order of the fundamental field. Consequently, the maximum energy that an electron wave packet can acquire from the field is estimated at around 4.0 eV. This value is much larger than the maximum phonon energy and exciton binding energy, demonstrating the Markov approximation is applicable [43]. Thus, we can introduce a characteristic constant dephasing rate to describe the scattering terms.

The commonly used phenomenological decoherence term which describes the exponential decay of off-diagonal elements of the density matrix has the form

$$\left[\frac{d\rho(\mathbf{k}, t)}{dt} \right]_{\text{decoh}} = -\frac{\rho_{ij}(\mathbf{k}, t)}{T_2} (1 - \delta_{ij}), \quad (23)$$

where T_2 represents the transverse dephasing time. We notice that Eq. (23) is not gauge invariant. In the velocity gauge (VG), another gauge-covariant form can be explicitly expressed as [46,47]

$$\frac{d\rho(\mathbf{k}, t)}{dt} \Big|_{\text{decoh}} = -\frac{1}{T_2 E_g^2} \{ H_0(\mathbf{k}) + \mathbf{A}(t) \cdot \mathbf{p}(\mathbf{k}), [H_0(\mathbf{k}) + \mathbf{A}(t) \cdot \mathbf{p}(\mathbf{k}), \rho(\mathbf{k}, t)] \}, \quad (24)$$

where T_2 is the phenomenological dephasing time and E_g has an energy dimension, which can be defined depending on the needs of specific situations. Here, we treat $T_2 E_g^2$ as an overall phenomenological dephasing factor.

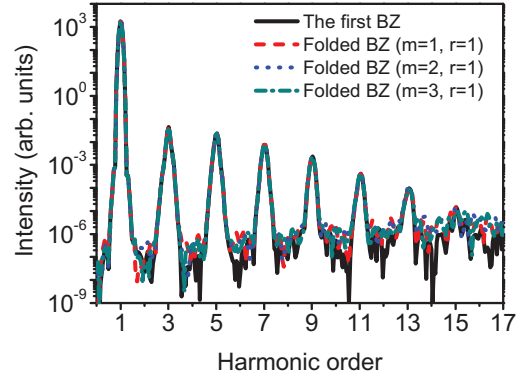


FIG. 8. Comparison of the harmonic spectrum in MLG calculated by choosing four different size unit cells, including a two-atom cell associated with the original first BZ in MLG (black solid), together with 28-atom, 76-atom, and 148-atom cells associated with the folded BZ whose shapes are the same as ($m = 1, r = 1$, red dashed), ($m = 2, r = 1$, blue dotted), and ($m = 3, r = 1$, olive dashed-dotted) tBLG, respectively. The pump pulse is linearly polarized along the Γ - K direction, with a central wavelength of 5900 nm, a duration of 90 fs, and a peak intensity of $3 \times 10^{12} \text{ W/cm}^2$. The dephasing time is $T_2 = 10 \text{ fs}$.

Our theoretical model supports the choice of arbitrary unit cells containing different carbon atom numbers, as long as they capture the system's periodicity. The larger unit cell can lead to more energy bands in the smaller folded BZ. Since the transverse relaxation process is related with two different bands via the off-diagonal elements of the density matrix, it is first necessary to examine the self-consistency of the model when the decoherence term is introduced. We have calculated the HHG spectrum from MLG with several unit cells, corresponding to the folded BZ of different sizes in the reciprocal space. Besides the original two-atom unit cell for the MLG, for comparison we also choose several unit cells the same as tBLG described by different m and r parameters, including a 28-atom unit cell for $m = 1$ and $r = 1$, a 76-atom unit cell for $m = 2$ and $r = 1$, and a 148-atom unit cell for $m = 3$ and $r = 1$. The calculation is performed by only keeping the bottom-layer Hamiltonian and removing the interlayer and top-layer Hamiltonian from our models. Two different relaxation expressions, Eqs. (23) and (24), are, respectively, incorporated into Eq. (9). Referring to the case of graphene where the typical dephasing time is found in a 10–100 fs range [48], $T_2 = 10 \text{ fs}$ is applied for Eq. (23) and $T_2 E_g^2 = 10 \text{ fs eV}^2$ is applied for Eq. (24) to illustrate the situation. A 90-fs duration driving pulse with a central wavelength of 5900 nm and a peak intensity of $3 \times 10^{12} \text{ W/cm}^2$ is employed. It turns out that the calculated HHG spectrum with different BZs are almost identical in both cases. Here, we only show the result of using Eq. (23) in Fig. 8, indicating that our model will not produce different results for the variation of energy band numbers in the folded BZ.

In order to reveal the essentials of the relaxation effect, we choose the minimal structure of tBLG with $\theta \approx 21.8^\circ$ to calculate the harmonic spectrum. Figures 9(a) and 9(b) exhibit the HHG efficiency ratio $R_N(\theta)$ between tBLG and MLG as a function of the dephasing time T_2 (or $T_2 E_g^2$) for HH3

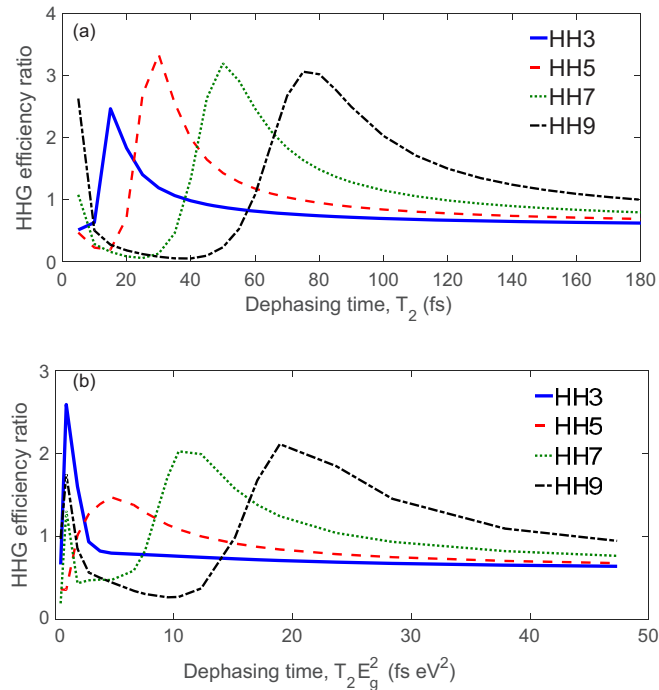


FIG. 9. The HHG efficiency ratio $R_N(\theta)$ in tBLG ($\theta \approx 21.8^\circ$) as a function of dephasing time for the HH3 (blue solid), HH5 (red dashed), HH7 (olive dot), and HH9 (black dashed-dotted), obtained from two different relaxation operators: (a) the gauge-variant decoherence term Eq. (23) and (b) the gauge-covariant form Eq. (24). Laser parameters are the same as in Fig. 8.

(blue solid), HH5 (red dashed), HH7 (green dotted), and HH9 (black dashed-dotted), obtained from two different relaxation operators: (a) the gauge-variant decoherence term Eq. (23) and (b) the gauge-covariant form Eq. (24). Both tBLG and MLG include the dephasing process. As shown in Fig. 9, the four characteristic curves of different orders appear to have a similar trend. The HHG efficiency ratio first reaches a sharp peak and then drops to a stable value, as the dephasing time increases. The dramatic dependence of $R_N(\theta)$ on T_2 (or $T_2 E_g^2$) indicates that the dephasing time has a great influence on the HHG efficiency ratio. In other words, the impact of ultrafast decoherence on HHG is quite different for the tBLG and MLG.

In addition, the four characteristic curves of different orders are separated from each other fairly well along the horizontal axis. The peak position of characteristic curves shifts toward a larger T_2 (or $T_2 E_g^2$) value with increasing the harmonic order. Another feature in Fig. 9 is that the curve changes more smoothly on both sides of the peak for the higher order. We can interpret this point according to the recollision model of HHG. When electron-hole recombination leads to photon emission, it takes more time to generate the higher-harmonic photon. The characteristic time for the higher harmonics is longer than the lower one, suggesting an insensitive dependence of the higher harmonics on dephasing time T_2 . As a result, the T_2 -dependent characteristic curve of higher-order harmonics possesses a slower rising and falling edge around the peak position, as shown in Fig. 9. Finally, we point out that although the exact value of the HHG effi-

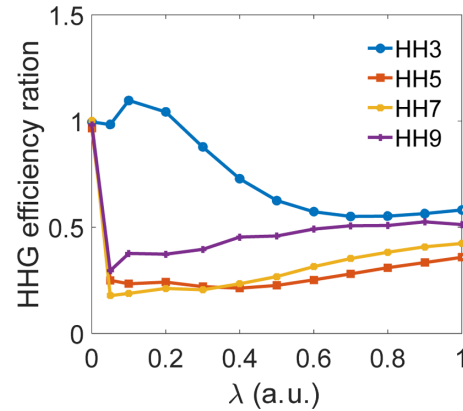


FIG. 10. HHG efficiency ratio $R_N(\theta)$ as a function of the inter-layer decay length λ , calculated for the HH3 (blue big dots), HH5 (red squares), HH7 (yellow small dots), and HH9 (purple pluses). Laser parameters are the same as in Fig. 7 and the dephasing time T_2 is set to 10 fs.

ciency ratio is a little different for using different decoherence expression Eqs. (23) and (24), the typical features of the characteristic curves are the same.

Equation (8) indicates that the interlayer interaction in our model is controlled by the decay length λ . We can investigate the effect of interlayer coupling by varying this parameter. Figure 10 shows the HHG efficiency ratio $R_N(\theta)$ as a function of λ , calculated for HH3 (blue big dots), HH5 (red squares), HH7 (yellow small dots), and HH9 (purple pluses). It is found from Fig. 10 that $R_N(\theta)$ at each harmonic order has its own dependence form on λ . Especially for HH3, the $R_N(\theta)$ is sensitive to λ . For all harmonic orders, as expected, the HHG efficiency ratio is equal to 1 when the two layers are decoupled ($\lambda = 0$). The interlayer interaction for $\lambda > 0$ can modulate the harmonic process, causing variations in emission efficiency.

D. Retrieval of the dephasing time T_2 and interlayer decay parameter λ

It is well known that the dephasing time T_2 is an important parameter and can usually be obtained by typical photon echo or electron diffraction experiments. Also, the decay length of the electron hopping λ needs careful consideration among all band structure parameters of graphitic systems and, in particular, there is a demand for the prediction of a fine λ value in tBLG. Figures 9 and 10 suggest that the HHG efficiency ratio can be regarded as the information carrier of the dephasing time T_2 and decay parameter λ . Consequently, it is possible to find an all-optical method for reconstructing T_2 and λ from the observed high-harmonic spectrum.

It is worth pointing out that the reconstruction of dephasing time is applicable as long as decoherence information can be well mapped onto the difference among the HHG efficiency ratios of different orders. Indeed, this difference exists for using both relaxation operators, as shown in Fig. 9. Thus the reconstruction validity is equivalent in these two cases. Here we choose Eq. (23) to illustrate the reconstruction process and demonstrate the algorithm convergence due to its low computational cost.

In order to facilitate a description of the algorithm, we assume the original $T_2^0 = 10$ fs and $\lambda^0 = 0.27$ Å as target parameters to be reconstructed. The corresponding data of the HHG efficiency ratio for four orders, considered as a “simulated experiment,” can be directly extracted from data points at $T_2 = 10$ fs in Fig. 9(a). We denote simulated experimental data as R_N^0 , which is known in advance. Our goal is to retrieve T_2 and λ by making use of R_N^0 and some other parameters such as laser intensity and pulse duration that can be measured in the experiment.

For the trial parameters T_2^t and λ^t , the reconstructed HHG efficiency ratio which is obtained by our theoretical model is denoted as $R_N^t(T_2^t, \lambda^t)$. For a fixed harmonic order N , we can define the difference between the original and reconstructed efficiency ratio as

$$\delta_N = |R_N^t(T_2^t, \lambda^t) - R_N^0|. \quad (25)$$

By making full use of the information on four harmonic orders, we further introduce the mean square error of reconstruction:

$$\Delta_4 = \sqrt{\delta_3^2 + \delta_5^2 + \delta_7^2 + \delta_9^2}/4. \quad (26)$$

The reconstruction procedure is based on searching two-dimensional parameter space (T_2^t, λ^t) that minimizes Δ_4 , which is implemented by the SIMPLEX algorithm of Nelder and Mead [49]. However, the optimized solution determined by our algorithm is sensitive to the initial “guess” value and easily falls into the local optimum. We thus select a set of initial values to run the optimal algorithm, which will generate a sequence of local optimal solutions (T_2^t, λ^t) and their corresponding Δ_4 . If these solutions, which are sorted by the corresponding Δ_4 in descending order, can converge to a fixed value, we take this global optimal one as the retrieved result.

Specifically, we use 24 sets of initial values composed of

$$T_2^i = [0, 5, 15, 20] \text{ fs} \otimes \lambda^i = [0, 0.2, 0.4, 0.6, 0.8, 1] \text{ a.u.} \quad (27)$$

in our calculation. For each initial value, the optimization iteration process stops when the SIMPLEX size drops to 10^{-2} . The local optimal solutions (T_2, λ, Δ_4) corresponding to the 24 initial sets are plotted in Fig. 11(a). For better visualization, projection of local solutions on the T_2 - Δ_4 plane and the λ - Δ_4 plane is shown in Figs. 11(b) and 11(c), respectively. One can see that good convergence is achieved to generate the global optimal solution $T_2 = 9.9$ fs and $\lambda = 0.49$ a.u. = 0.26 Å, which matches the original value very well. This excellent agreement of reconstructed results manifests that our method for measuring dephasing time and interlayer decay parameter based on the HHG is feasible.

The reconstruction method is dependent on the pulse intensity and duration, which are assumed to be accurate in the above calculation. To make the simulation more realistic, it is necessary to extend our study in the case of considering experimental uncertainty of laser parameters. As guidance, the influence of the laser peak intensity and pulse duration on the HHG efficiency ratio are explored and the results for HH3 (blue solid), HH5 (red dashed), HH7 (green dotted), and HH9 (black dashed-dotted) are reported in Figs. 12(a) and 12(b). It is found that the HH3 and HH9 efficiency ratios are deeply

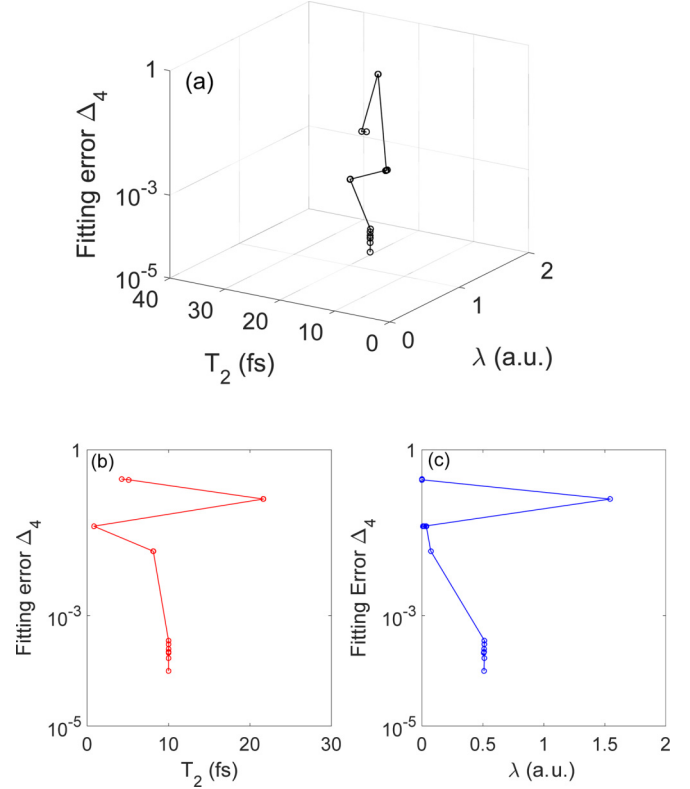


FIG. 11. The optimization process for retrieving the dephasing time T_2 and interlayer decay parameter λ . (a) The 24 sets of local optimal solutions (T_2, λ, Δ_4) from different initial values, sorted by the Δ_4 in descending order. (b) Projection of panel (a) on the T_2 - Δ_4 plane. (c) Projection of panel (a) on the λ - Δ_4 plane.

modulated by the peak intensity and pulse duration, while HH5 and HH7 change slightly. This feature suggests that HH3 and HH9 information should be removed in the reconstruction process for improving antinoise ability. We define a new mean square error of reconstruction only using HH5 and HH7 as

$$\Delta_2 = \sqrt{\delta_5^2 + \delta_7^2}/2. \quad (28)$$

We also introduce to the original peak intensity and pulse duration 20% uncertainty error, which is sufficiently larger for the experimental measurement. The same optimization

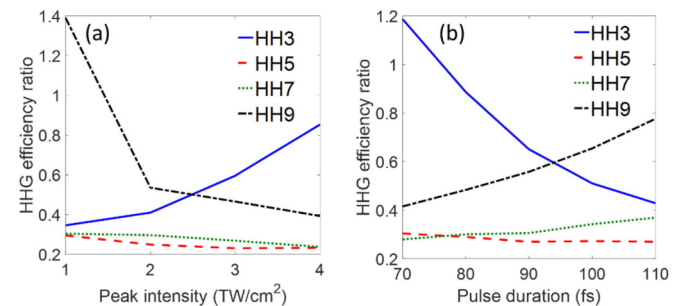


FIG. 12. The HHG efficiency ratio $R_N(\theta)$ as a function of (a) the peak intensity and (b) the pulse duration, calculated for HH3 (blue solid), HH5 (red dashed), HH7 (olive dot), and HH9 (black dashed-dotted). The original $T_2^0 = 10$ fs and $\lambda^0 = 0.27$ Å are used.

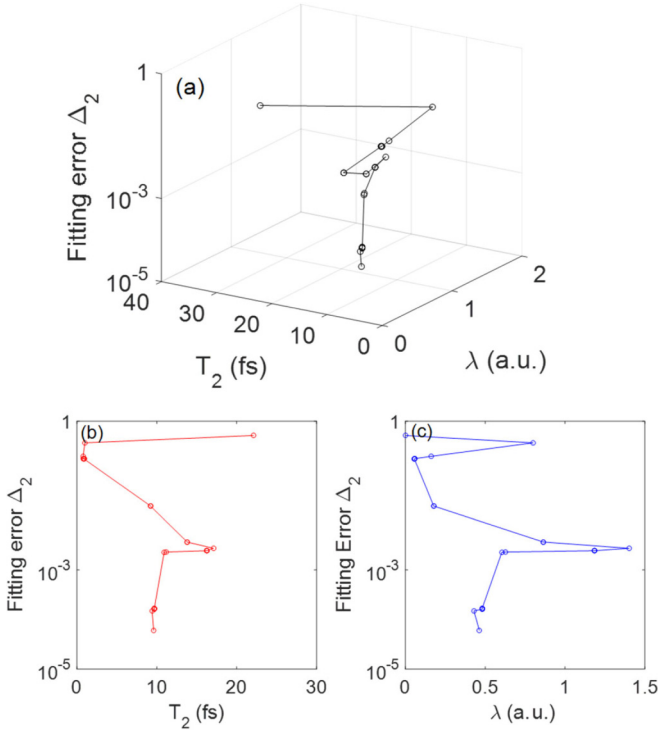


FIG. 13. The optimization process for retrieving the dephasing time T_2 and interlayer decay parameter λ , in the case of introducing to the original peak intensity and pulse duration 20% uncertainty error. (a) The 24 sets of local optimal solutions (T_2, λ, Δ_2) from different initial values, sorted by the Δ_2 in descending order. (b) Projection of panel (a) on the T_2 - Δ_2 plane. (c) Projection of panel (a) on the λ - Δ_2 plane.

algorithm is performed to minimize Δ_2 , except for using the modified intensity and duration instead of the original ones. Figure 13(a) shows the local optimal solutions (T_2, λ, Δ_2) , whose projection on the T_2 - Δ_2 plane and the λ - Δ_2 plane are shown in Figs. 13(b) and 13(c), respectively. It is found from Fig. 13 that we also get the convergence value $T_2 = 9.6$ fs and $\lambda = 0.46$ a.u. = 0.24 \AA . The relative reconstruction error is 4% for T_2 and 11% for λ .

Finally, the reconstruction algorithm is further discussed by introducing uniformly distributed random noise onto the HHG signal. By making use of a random number generator, we introduce to the original MLG and tBLG HHG spectrogram a uniform noise with the amplitude equal to $\pm 10\%$ of the harmonic intensity for HH5 and HH7. A $\pm 10\%$ uncertainty error in the original peak intensity and pulse duration is also included. The reconstruction process is the same as the one used in obtaining Fig. 13. The same optimization algorithm is performed to minimize Δ_2 . We can get the convergence values $T_2 = 13.8$ fs and $\lambda = 0.80$ a.u. = 0.424 \AA . The reconstructed T_2 deviation from the original value 10 fs is 3.8 fs, which is much less than half of the optical cycle $T_0/2 = 9.83$ fs. Hence this relative error is tolerable. To evaluate the efficacy of the reconstructed decay parameter, we apply it to calculate the energy bands of tBLG. It is found that the recalculated energy bands with the reconstructed parameter $\lambda = 0.424 \text{ \AA}$ are almost identical to the original ones given in Fig. 14,

demonstrating the reconstructed decay parameter is reasonable. It is obvious that for both the ideal and noise-containing case a satisfactory reconstruction result can be achieved. Therefore we can conclude that our method can produce solid results.

IV. CONCLUSIONS

In summary, we have theoretically investigated HHG in tBLG, arising from the nonlinear optical response to an intense MIR field. In order to facilitate theoretical calculations, we mainly consider the commensurate structure of tBLG which preserves the translation symmetry. The electronic states of tBLG are constructed by the tight-binding model, which is combined to time-dependent density-matrix equations in the velocity gauge for describing strong-field electron dynamics. Our model can avoid the phase continuous requirement of transition dipole moments in the momentum space, and include the Pauli blocking of interband transitions.

We find that for a wide range of laser intensities the model can lead to a clear and discrete high-harmonic spectrum. In particular, under the strong pump intensity that is commonly used in the experiment for 2D materials, the parallel harmonic emission is dominate for arbitrary crystal orientation, so that we can safely ignore the perpendicular component of high harmonics. We analyze the dependence of harmonic yield on the crystal orientation for different bilayer graphene systems. The conventional AA and AB stacking bilayer graphene exhibits the same crystal-orientation-dependent modulation as MLG. When the pump laser is polarized along the Γ - K direction, the maximal harmonic yield can be achieved. In contrast, the maximal harmonic yield in tBLG occurs for the driving polarization along the Γ - M direction, which can be explained by the interference of harmonic emission from each layer of tBLG. In addition, it is found that in the absence of the dephasing process the harmonic emission efficiency per layer in tBLG is significantly suppressed for the twisted angle around 10° owing to the competition between multiband effects at small angles and Fermi velocity decrease at large angles. Moreover, we demonstrate that the HHG efficiency ratio between tBLG and MLG for a specific harmonic order can be controlled by the dephasing time T_2 and interlayer hopping decay length λ . This property provides the opportunity to encode these parameters into the high-harmonic spectrum, thus suggesting an all-optical method to measure the two parameters. Making use of an optimization algorithm, we show the feasibility for simultaneous reconstruction of T_2 and λ even under some experimental uncertainty. Hence, our work is a step toward describing the dynamics of ultrafast electrons in tBLG by high-order harmonic spectroscopy.

ACKNOWLEDGMENTS

This work was supported by the National Natural Science Foundation of China (Grants No. 61690223, No. 11774363, No. 11561121002, No. 61521093, and No. 11127901) and the Strategic Priority Research Program of the Chinese Academy of Sciences (Grant No. XDB16).

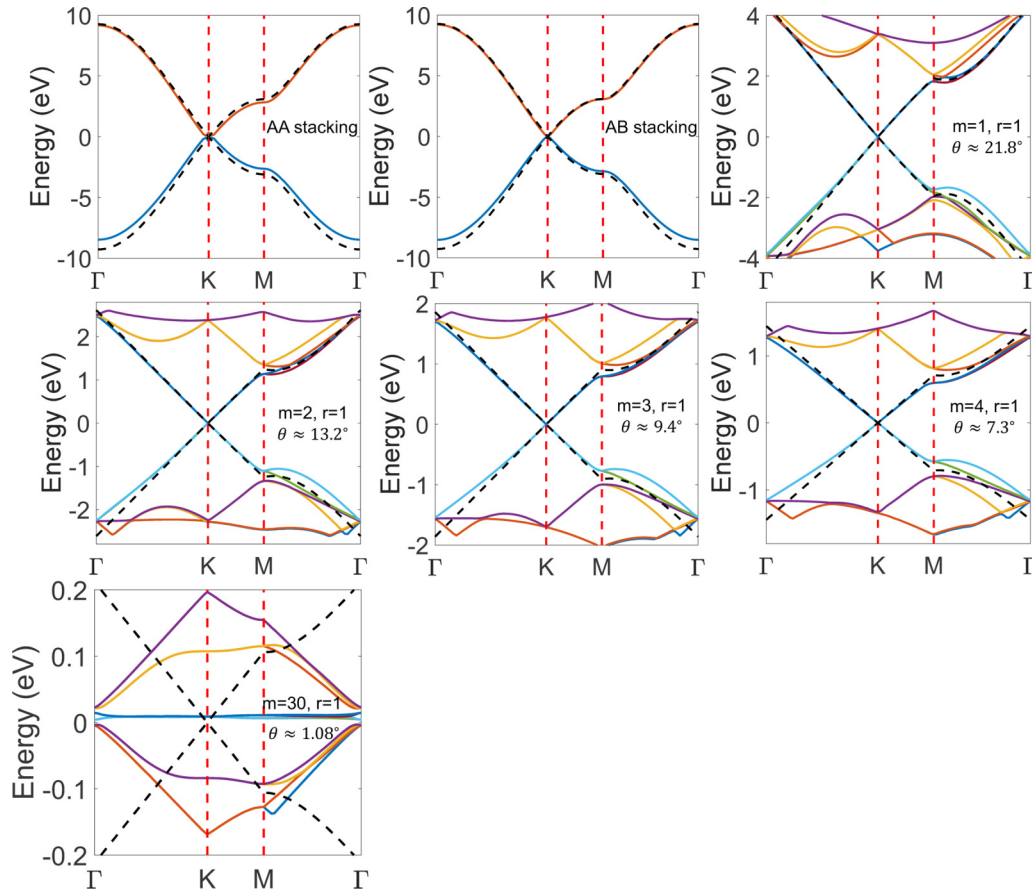


FIG. 14. Energy bands of different bilayer graphene systems. The black dashed line in each panel represents the MLG energy band for comparison.

APPENDIX: BAND STRUCTURES OBTAINED BY TIGHT-BINDING MODEL

In order to examine the TB model and our numerical code, we calculate energy bands of several tBLG structures with the $r = 1$ family, as shown in Fig. 14. Although complete bands are obtained, we only plot a few of them around the Fermi level for better observation. One can find that the distribution of energy bands near the Fermi level becomes richer with

decreasing the twisted angle (note different scales on each vertical axis). This originates from the energy band folded in the smaller BZ for the larger superlattice. For each panel in Fig. 14, we also plot the upper valence and the lowest conduction band of MLG by a black dashed line in the corresponding folded BZ. The first magic angle, $\theta \approx 1.08^\circ$, at which band flattening occurs has been successfully captured, as given by the last panel in Fig. 14.

- [1] S. Ghimire, A. D. DiChiara, E. Sistrunk, P. Agostini, L. F. DiMauro, and D. A. Reis, Observation of high-order harmonic generation in a bulk crystal, *Nat. Phys.* **7**, 138 (2011).
- [2] O. Schubert, M. Hohenleutner, F. Langer, B. Urbanek, C. Lange, U. Huttner, D. Golde, T. Meier, M. Kira, S. W. Koch, and R. Huber, Sub-cycle control of terahertz high-harmonic generation by dynamical Bloch oscillations, *Nat. Photon.* **8**, 119 (2014).
- [3] T. T. Luu, M. Garg, S. Y. Kruchinin, A. Moulet, M. T. Hassan, and E. Goulielmakis, Extreme ultraviolet high-harmonic spectroscopy of solids, *Nature (London)* **521**, 498 (2015).
- [4] H. Liu, Y. Li, Y. S. You, S. Ghimire, T. F. Heinz, and D. A. Reis, High-harmonic generation from an atomically thin semiconductor, *Nat. Phys.* **13**, 262 (2016).
- [5] G. Ndashimiye, S. Ghimire, M. Wu, D. A. Browne, K. J. Schafer, M. B. Gaarde, and D. A. Reis, Solid-state harmonics beyond the atomic limit, *Nature (London)* **534**, 520 (2016).
- [6] N. Yoshikawa, T. Tamaya, and K. Tanaka, High-harmonic generation in graphene enhanced by elliptically polarized light excitation, *Science* **356**, 736 (2017).
- [7] Y. S. You, Y. Yin, Y. Wu, A. Chew, X. Ren, F. Zhuang, S. Gholam-Mirzaei, M. Chini, Z. Chang, and S. Ghimire, High-harmonic generation in amorphous solids, *Nat. Commun.* **8**, 724 (2017).
- [8] H. Kim, S. Han, Y. W. Kim, S. Kim, and S.-W. Kim, Generation of coherent extreme-ultraviolet radiation from bulk sapphire crystal, *ACS Photon.* **4**, 1627 (2017).
- [9] K. Kaneshima, Y. Shinohara, K. Takeuchi, N. Ishii, K. Imasaka, T. Kaji, S. Ashihara, K. L. Ishikawa, and J.

- Itatani, Polarization-Resolved Study of High Harmonics From Bulk Semiconductors, *Phys. Rev. Lett.* **120**, 243903 (2018).
- [10] R. E. F. Silva, I. V. Blinov, A. N. Rubtsov, O. Smirnova, and M. Ivanov, High-harmonic spectroscopy of ultrafast many-body dynamics in strongly correlated systems, *Nat. Photon.* **12**, 266 (2018).
- [11] G. Vampa, T. J. Hammond, N. Thiré, B. E. Schmidt, F. Légaré, C. R. McDonald, T. Brabec, D. D. Klug, and P. B. Corkum, All-Optical Reconstruction of Crystal Band Structure, *Phys. Rev. Lett.* **115**, 193603 (2015).
- [12] T. T. Luu and H. J. Wörner, Measurement of the Berry curvature of solids using high-harmonic spectroscopy, *Nat. Commun.* **9**, 916 (2018).
- [13] M. Garg, M. Zhan, T. T. Luu, H. Lakhota, T. Klostermann, A. Guggenmos, and E. Goulielmakis, Multi-petahertz electronic metrology, *Nature (London)* **538**, 359 (2016).
- [14] O. Neufeld, D. Podolsky, and O. Cohen, Floquet group theory and its application to selection rules in harmonic generation, *Nat. Commun.* **10**, 405 (2019).
- [15] F. Langer, M. Hohenleutner, U. Huttner, S. W. Koch, M. Kira, and R. Huber, Symmetry-controlled temporal structure of high-harmonic carrier fields from a bulk crystal, *Nat. Photon.* **11**, 227 (2017).
- [16] C. Liu, Y. Zheng, Z. Zeng, and R. Li, Driving-laser ellipticity dependence of high-order harmonic generation in graphene, *Phys. Rev. A* **97**, 063412 (2018).
- [17] X. Zhang, J. Li, Z. Zhou, S. Yue, H. Du, L. Fu, and H.-G. Luo, Ellipticity dependence transition induced by dynamical Bloch oscillations, *Phys. Rev. B* **99**, 014304 (2019).
- [18] Y. Gao, Y. Zhang, and D. Xiao, Tunable Layer Circular Photogalvanic Effect in Twisted Bilayers, *Phys. Rev. Lett.* **124**, 077401 (2020).
- [19] M. J. Park, Y. Kim, G. Y. Cho, and S. Lee, Higher-Order Topological Insulator in Twisted Bilayer Graphene, *Phys. Rev. Lett.* **123**, 216803 (2019).
- [20] Y. Cao, V. Fatemi, A. Demir, S. Fang, S. L. Tomarken, J. Y. Luo, J. D. Sanchez-Yamagishi, K. Watanabe, T. Taniguchi, E. Kaxiras, R. C. Ashoori, and P. Jarillo-Herrero, Correlated insulator behaviour at half-filling in magic-angle graphene superlattices, *Nature (London)* **556**, 80 (2018).
- [21] E. J. Mele, Commensuration and interlayer coherence in twisted bilayer graphene, *Phys. Rev. B* **81**, 161405(R) (2010).
- [22] J. M. B. Lopes dos Santos, N. M. R. Peres, and A. H. Castro Neto, Graphene Bilayer with a Twist: Electronic Structure, *Phys. Rev. Lett* **99**, 256802 (2007).
- [23] G. Vampa, C. R. McDonald, G. Orlando, D. D. Klug, P. B. Corkum, and T. Brabec, Theoretical Analysis of High-Harmonic Generation in Solids, *Phys. Rev. Lett.* **113**, 073901 (2014).
- [24] T. T. Luu and H. J. Wörner, High-order harmonic generation in solids: A unifying approach, *Phys. Rev. B* **94**, 115164 (2016).
- [25] C. Yu, S. Jiang, T. Wu, G. Yuan, Z. Wang, C. Jin, and R. Lu, Two-dimensional imaging of energy bands from crystal orientation dependent higher-order harmonic spectra in *h*-BN, *Phys. Rev. B* **98**, 085439 (2018).
- [26] J. Li, X. Zhang, S. Fu, Y. Feng, B. Hu, and H. Du, Phase invariance of the semiconductor Bloch equations, *Phys. Rev. A* **100**, 043404 (2019).
- [27] L. Yue and M. B. Gaarde, Structure gauges and laser gauges for the semiconductor Bloch equations in high-order harmonic generation in solids, *Phys. Rev. A* **101**, 053411 (2020).
- [28] S. Jiang, J. Chen, H. Wei, C. Yu, R. Lu, and C. D. Lin, Role of the Transition Dipole Amplitude and Phase on The Generation of Odd and Even High-Order Harmonics in Crystals, *Phys. Rev. Lett.* **120**, 253201 (2018).
- [29] S. Jiang, C. Yu, J. Chen, Y. Huang, R. Lu, and C. D. Lin, Smooth periodic gauge satisfying crystal symmetry and periodicity to study high-harmonic generation in solids, *Phys. Rev. B* **102**, 155201 (2020).
- [30] C. Liu, Y. Zheng, Z. Zeng, and R. Li, Polarization-resolved analysis of high-order harmonic generation in monolayer MoS₂, *New J. Phys.* **22**, 073046 (2020).
- [31] T. N. Ikeda, High-order nonlinear optical response of a twisted bilayer graphene, *Phys. Rev. Res.* **2**, 032015(R) (2020).
- [32] M. Korbman, S. Yu. Kruchinin, and V. S. Yakovlev, Quantum beats in the polarization response of a dielectric to intense few-cycle laser pulses, *New J. Phys.* **15**, 013006 (2013).
- [33] V. M. Axt and T. Kuhn, Femtosecond spectroscopy in semiconductors: A key to coherences, correlations and quantum kinetics, *Rep. Prog. Phys.* **67**, 433 (2004).
- [34] J. M. B. Lopes dos Santos, N. M. R. Peres, and A. H. Castro Neto, Continuum model of the twisted graphene bilayer, *Phys. Rev. B* **86**, 155449 (2012).
- [35] H. A. Le and V. N. Do, Electronic structure and optical properties of twisted bilayer graphene calculated via time evolution of states in real space, *Phys. Rev. B* **97**, 125136 (2018).
- [36] X. Lin and D. Tománek, Minimum model for the electronic structure of twisted bilayer graphene and related structures, *Phys. Rev. B* **98**, 081410(R) (2018).
- [37] T. G. Pedersen, K. Pedersen, and T. B. Kriestensen, Optical matrix elements in tight-binding calculations, *Phys. Rev. B* **63**, 201101(R) (2001).
- [38] Y. Bai, F. Fei, S. Wang, N. Li, X. Li, F. Song, R. Li, Z. Xu, and P. Liu, High-harmonic generation from topological surface states, *Nat. Phys.* **17**, 311 (2021).
- [39] A. O. Sboychakov, A. L. Rakhmanov, A. V. Rozhkov, and F. Nori, Electronic spectrum of twisted bilayer graphene, *Phys. Rev. B* **92**, 075402 (2015).
- [40] A. H. Castro Neto, F. Guinea, N. M. R. Peres, K. S. Novoselov, and A. K. Geim, The electronic properties of graphene, *Rev. Mod. Phys.* **81**, 109 (2009).
- [41] K. L. Ishikawa, Nonlinear optical response of graphene in time domain, *Phys. Rev. B* **82**, 201402(R) (2010).
- [42] J. D. Cox, A. Marini, and F. J. G. de Abajo, Plasmon-assisted high-harmonic generation in graphene, *Nat. Commun.* **8**, 14380 (2017).
- [43] S. Y. Kruchinin, Non-Markovian pure dephasing in a dielectric excited by a few-cycle laser pulse, *Phys. Rev. A* **100**, 043839 (2019).
- [44] H. Patel, L. Huang, C. J. Kim, J. Park, and M. W. Graham, Stacking angle-tunable photoluminescence from interlayer exciton states in twisted bilayer graphene, *Nat. Commun.* **10**, 1445 (2019).
- [45] M. Lamparski, B. Van Troeye, and V. Meunier, Soliton signature in the phonon spectrum of twisted bilayer graphene, *2D Mater.* **7**, 025050 (2020).

- [46] M. S. Wismer and V. S. Yakovlev, Gauge-independent decoherence models for solids in external fields, *Phys. Rev. B* **97**, 144302 (2018).
- [47] L. H. Thong, C. Ngo, H. T. Duc, X. Song, and T. Meier, Microscopic analysis of high harmonic generation in semiconductors with degenerate bands, *Phys. Rev. B* **103**, 085201 (2021).
- [48] M. Breusing, S. Kuehn, T. Winzer, E. Malić, F. Milde, N. Severin, J. P. Rabe, C. Ropers, A. Knorr, and T. Elsaesser, Ultrafast nonequilibrium carrier dynamics in a single graphene layer, *Phys. Rev. B* **83**, 153410 (2011).
- [49] <http://www.gnu.org/software/gsl/>.